iScience

CellPress

Article

Nontemplating Porous Carbon Material from Polyphosphamide Resin for Supercapacitors

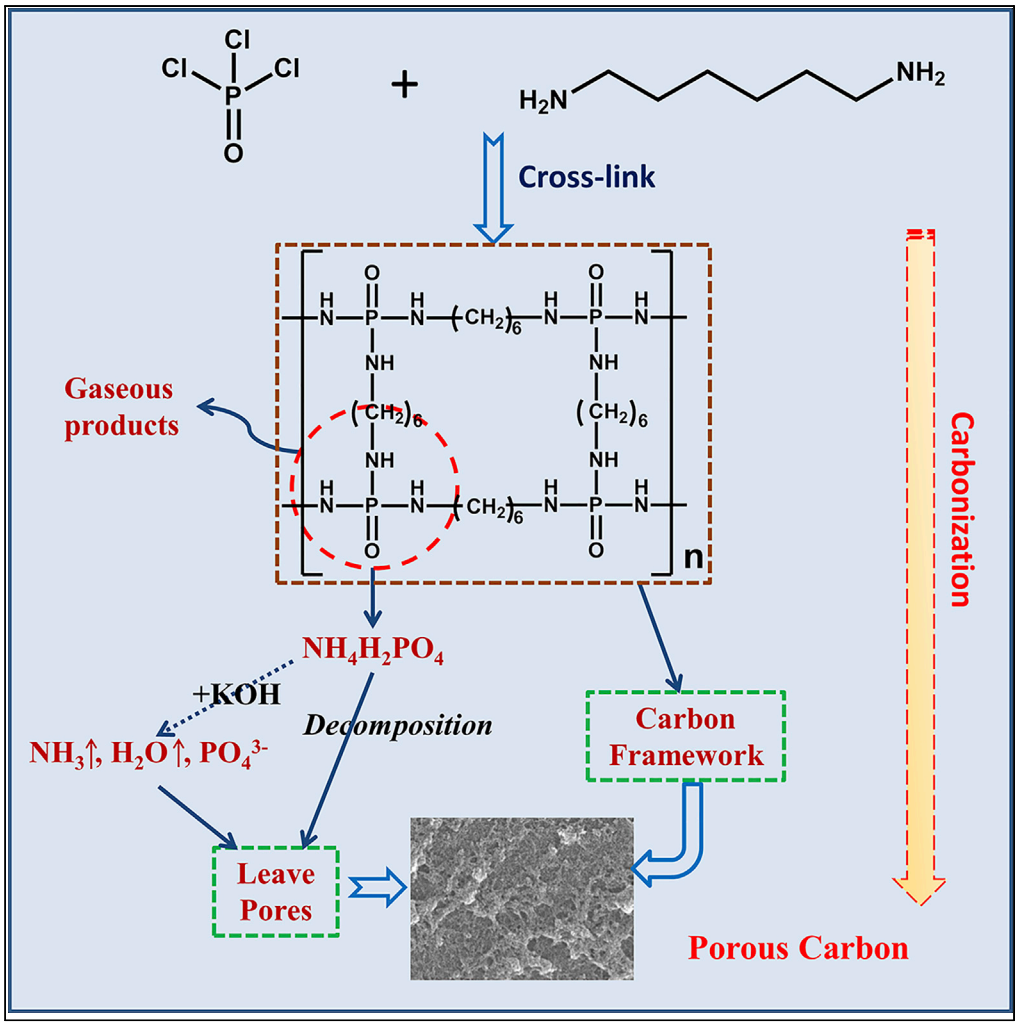

Bin-Hai Cheng, Fan-Xin Zeng, Wen-Jing Chen, Hui-Yuan Cheng, Raymond J. Zeng, Hong Jiang

jhong@ustc.edu.cn

HIGHLIGHTS

A cross-linking polyphosphamide resin with defined N and P structure is synthesized

A PCM prepared form the special resin exhibited high supercapacitor performance

The pore formation mechanism of the PCM was investigated

Cheng et al., iScience *12*, 204–215
February 22, 2019
https://doi.org/10.1016/j.isci.2019.01.016

iScience

CellPress

Article

Nontemplating Porous Carbon Material from Polyphosphamide Resin for Supercapacitors

Bin-Hai Cheng,[1,2] Fan-Xin Zeng,[2] Wen-Jing Chen,[2] Hui-Yuan Cheng,[2] Raymond J. Zeng,[1,2] and Hong Jiang[2,3,*]

SUMMARY

The nontemplating preparation of porous carbon materials by using specially designed polymer precursors for supercapacitor is attracting considerable research attention because of the more controllable frame structure and easier processes than templating methods. Herein, a deliberately designed cross-linking polyphosphamide resin with defined N and P structure is synthesized and then carbonized to obtain porous carbon material. The as-obtained porous carbon material has a specific surface area of 2,620 m^2 g^{-1}, high porosity of 1.49 cm^3 g^{-1}, and well-distributed micro/mesoporous carbon structure. Different from activation by post-added $NH_4H_2PO_4$, the confined N and P in the polymer frame are confirmed to play an important role in pore structure development by forming *in situ* highly dispersed $NH_4H_2PO_4$ during carbonization. When evaluated as the electrode material for supercapacitors, the polyphosphamide-resin-based porous carbon material demonstrates excellent capacitance (440 F g^{-1} under 0.5 A g^{-1}) and high stability (retention of 93% over 10,000 cycles).

INTRODUCTION

With the depletion of conventional energy resources, green and sustainable energy conversion and storage technologies are attracting more and more attention. Among various energy storage devices, supercapacitors have their advantages of high charge-discharge rate, long cycle life, high energy conversion efficiency, etc. (Wang et al., 2012). According to the energy storage mechanisms, supercapacitors can be categorized into electrical double-layer capacitors (EDLCs) and pseudocapacitors (Salanne et al., 2016). EDLCs store energy through ion adsorption-desorption at the electrode-electrolyte interfaces. The typical materials for EDLCs always have high specific surface area (SSA), such as porous carbon (Yao et al., 2018), carbon nanotube (Yu et al., 2014), and graphene (Strauss et al., 2018). Pseudocapacitors store energy by reversible faradaic reactions of the electrode materials, such as $Ni(OH)_2$ (Su et al., 2014), MnO_2 (Wang et al., 2015), and V_2O_5 (Wang et al., 2018a). Up to now, EDLCs still hold the dominant market position owing to their low cost and high reliability.

Porous carbon materials (PCMs) are widely used as electrode materials in supercapacitors, especially EDLCs, owing to their stable physical and chemical properties, large SSA, controllable pore structure, high electronic conductivity, and low cost (Liu et al., 2017; Simon and Gogotsi, 2008; Zhai et al., 2011; Zhang and Zhao, 2009). The capacitance of PCM-based supercapacitors is mainly determined by the SSA and pore structure of PCMs, providing ion storage interface and facilitating the ion transportation, respectively (Chmiola et al., 2006a; Pandolfo and Hollenkamp, 2006). Therefore much research has been devoted to optimize the pore structure by preparing ordered and hierarchical (micropores and mesopores) PCMs on the premise of remaining large SSA to enhance the EDLC capacity (Kondrat et al., 2012; Largeot et al., 2008; Qie et al., 2013; Tran and Kalra, 2013). Although metal-organic frameworks (Hu et al., 2010) and metal carbides (Chmiola et al., 2006b) have been used to prepare pore-controllable PCMs, organic polymers are promising precursors because they can be handily designed and synthesized with specific structures and composition; these features are important to obtain PCMs with the desired pore structure (Dutta et al., 2014; Wei et al., 2013; Xu et al., 2013; Zhong et al., 2012).

Polymerization of monomers for preparing organic polymers provides the possibility of tuning the final structures, during which monomers may be restricted to the specific space for *in situ* polymerization or self-assembly. For instance, Böttger-Hiller et al. used spherical SiO_2 particles as hard templates to allow *in situ* monomer polymerization and prepared hollow carbon spheres with porous shell by carbonization and washing of the templates (Böttger-Hiller et al., 2013). Using surfactants or block copolymers as soft

[1]School of Life Sciences, University of Science and Technology of China, Hefei, China

[2]CAS Key Laboratory of Urban Pollutant Conversion, Department of Chemistry, University of Science and Technology of China, Hefei, China

[3]Lead Contact

*Correspondence: jhong@ustc.edu.cn

https://doi.org/10.1016/j.isci.2019.01.016

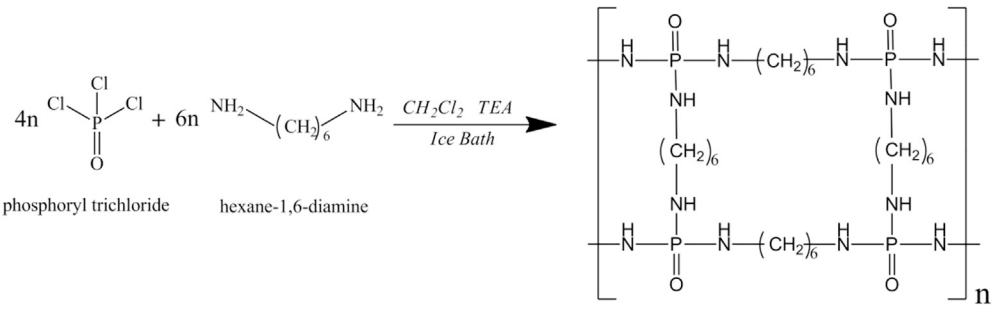

Scheme 1. Scheme for the PAR Synthesis

templating can direct the polymerization of monomers, and after drying and carbonization, PCMs can be obtained (Chuenchom et al., 2012). For instance, block copolymers, such as Pluronic F-127 ($EO_{106}PO_{70}EO_{106}$), are commonly used as structure-directing agents for the self-assembly of monomers (Hasegawa et al., 2016; Wang et al., 2018b; Xiong et al., 2017). Liang et al. reported that, by changing the mixture of F127, phloroglucinol, and formaldehyde and the processing conditions, different forms of fibers, sheets, films, and monoliths can be readily synthesized (Liang and Dai, 2006). Estevez et al. reported a dual-templating and post-activation strategy to prepare hierarchical porous carbon (Estevez et al., 2013). Combined ice-template and colloidal silica followed by physical activation was applied to generate interconnected macro-, meso-, and microporosity. However, most of the templates are rather expensive and nonrenewable, which limits their application.

In recent years, several studies focused on developing new methods from direct carbonization of special polymers without using any template (Hu et al., 2012; Zhang et al., 2013; Zhu et al., 2015). Porous structure can be formed by regulating the cross-linking style of the polymer or inserting specific elements into the framework. For instance, Puthusseri et al. reported a nontemplating method to synthesize interconnected microporous carbon material by direct pyrolysis of poly (acrylamide-*co*-acrylic acid) potassium salt without any additional activation. During the pyrolysis, the potassium in the polymer reacted with the carbon to form K_2CO_3, which creates pores in the carbon framework (Puthusseri et al., 2014). Sevilla et al. reported similar results by using potassium citrate as the precursor (Sevilla and Fuertes, 2014). Apart from K_2CO_3, chemical compounds, such as KOH, NH_3, and $NH_4H_2PO_4$, were also helpful in the formation of porous carbon (Krüner et al., 2018; Li et al., 2010; Wang and Kaskel, 2012; Zhou et al., 2015).

In this study, we proposed a nontemplating method to prepare PCM with high capacitance. We first designed and synthesized a hyper-cross-linked N, P-rich polymer containing the P–N groups, denoted as polyphosphamide resin (PAR). Hyper-cross-linked N, P-rich polymer with hierarchical framework can not only facilitate the formation of well-defined pore structure but also increase the SSA by activation of the formed N, P species (such as NH_3 and $NH_4H_2PO_4$). Afterward, the PAR was pyrolyzed and post-activated to prepare PCMs. The properties of PAR and the as-prepared PCM were characterized by Fourier transform infrared (FTIR) spectroscopy, X-ray photoelectron spectroscopy (XPS), Raman spectrum, scanning electron microscopy (SEM), etc. The electrochemical capacitance performance of the as-obtained PCMs was evaluated both in the three-electrode and two-electrode systems. The role of N, P in improving the PCM performance was also investigated.

RESULTS

Preparation of Polyphosphamide Resin

PAR was prepared according to our previous work (Zeng et al., 2011). The synthetic route of the PAR is shown in Scheme 1.

In the synthesis of PAR, N–P bonds were formed to link the phosphoryl trichloride and hexane-1,6-diamine. Phosphoryl trichloride acted as a center to connect three molecules of hexane-1,6-diamine, and the other head of hexane-1,6-diamine was bonded to another phosphoryl trichloride. Thus, a branch-like network grew. Therefore the $O{=}P{-}(N{-}C)_3$ structures were well-dispersed as nodes in the PAR network, as shown in Figure 1.

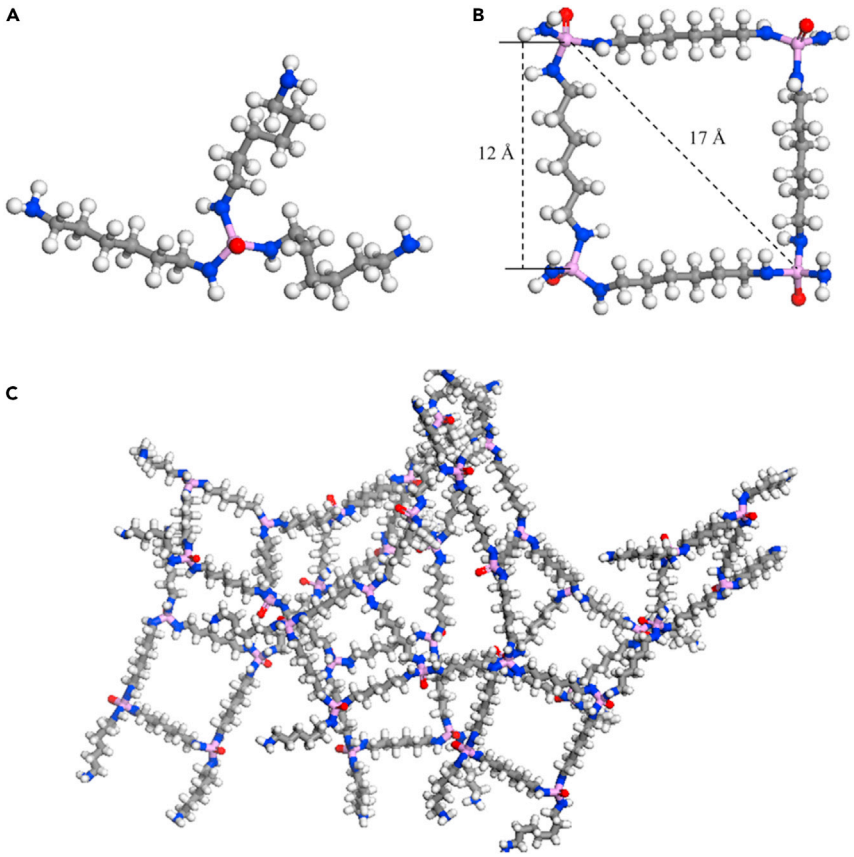

Figure 1. Simulated Molecular Model of PAR

(A) Formation of O=P–(N–C)$_3$ node with one phosphoryl trichloride molecule and three hexane-1,6-diamine molecules.

(B) Possible structural unit of PAR.

(C) Simulated molecular structure of PAR. Atoms involved in simulation: carbon, gray; nitrogen, blue; oxygen, red; phosphorus, pink; and hydrogen, white.

The FTIR spectrum of PAR is shown in Figure 2A. The broad band at 3,422 cm^{-1} indicated the existence of N–H. The doublet peaks occurring at 2,930 and 2,858 cm^{-1} were ascribed to the symmetric and asymmetric stretchings of alkyl C–H. The band at 1,640 cm^{-1} was the stretching of P=O. The peaks at 1,546 and 1,463 cm^{-1} were the deformation vibration of N–H and bending vibration of C–H, respectively. The peaks at 1,267 and 1,096 cm^{-1} were attributed to the symmetric and asymmetric stretching vibrations of C–N. Notably, the peak at 982 cm^{-1} indicated the presence of N–P. Furthermore, the XPS spectra shown in Figure S2 demonstrated the existence of N–P bonds. All these peaks found in the FTIR spectrum and XPS spectra suggested that the phosphoramide structure of the resin was formed, consistent with the initial design.

The thermal degradation behavior of PAR is shown in Figure 2B. Two major degradation peaks are shown in the differential thermal analysis curve (red line). One is from ~381°C to 495°C, with 18.6% loss of the total weight attributed to the decomposition of the P–N, C–N, and P=O groups. The other is from ~495°C to 779°C, with 52.1% loss of the total weight due to polymer carbonization (e.g., the cleavage of C–H and C–C bonds) to form the carbon framework.

Physicochemical Properties of PCMs

Based on the thermogravimetric analysis (TGA), the PAR was pyrolyzed under an Ar atmosphere to prepare PCM$_{PAR}$. The morphology and structure of PCM$_{PAR}$ were first examined by SEM and transmission electron microscopy (TEM). The SEM image shows that PCM$_{PAR}$ has rough surface with multiple micropores (Figure 3A). The TEM image exhibits large number of micropores in the inner structure of the material (Figures

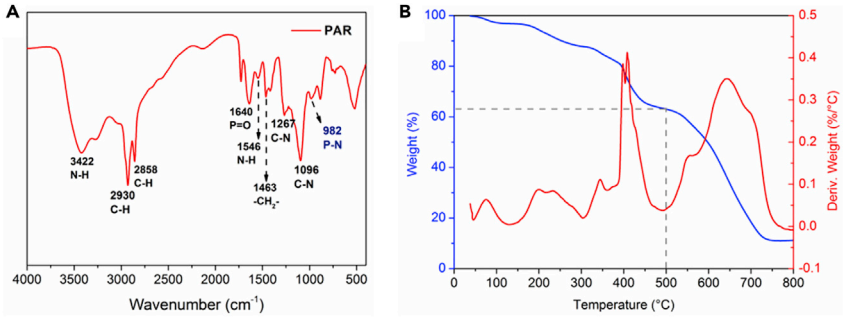

Figure 2. Materials Characterization of PAR

(A) FTIR spectrum of the PAR.

(B) TG-differential scanning calorimeter (DSC) curves of the PAR.

3B and S3), indicating that it is a porous material. The porous nature of PCM_{PAR} can enhance the performance of supercapacitor (Hou et al., 2015; Huang et al., 2016; Tian et al., 2015). N_2 adsorption-desorption method was used to analyze the SSA and pore texture of the PCMs. In Figure 3C, compared with PCM_{PFR}, PCM_{PAR} and PCM_{PFR+NP} exhibit a significant increase in volume when P/P_0 increases from 0 to 0.3. This phenomenon suggests that the curves are between types I and IV (IUPAC classification), which is attributed to the presence of certain mesopores in the materials (Tao et al., 2006). The result can also be proved by pore size distributions (Figure 3D), which indicates that all the PCMs possess a certain fraction of mesopores (>2 nm). The figure clearly shows that the micropores of PCMs concentrated at 1–3 nm along with a small proportion at approximately 0.5 nm. Notably, the proportion of mesopores showed an order of PCM_{PAR}>PCM_{PFR+NP}>PCM_{PFR}. The Brunauer–Emmett–Teller (BET) SSAs of PCM_{PAR}, PCM_{PFR}, and PCM_{PFR+NP} were 2,620, 2,233, and 3,062 $m^2\ g^{-1}$, respectively. The SSA, pore volume, and average pore size of the PCMs are summarized in Table 1.

Influence of the Precursor on the Formation of PCMs

To reveal the roles of nitrogen and phosphorus in the formation of special pore structure of PCM_{PAR}, PFR was selected as a common precursor to fabricate PCM_{PFR}, which contains no nitrogen and phosphorus. The transformation of N and P during the entire process was investigated to explore their effect on the formation of PCMs. The change of P content during the porous carbon preparation is shown in Figure 4A. Briefly, 13.2 wt % P in original PAR concentrated to 18.8 wt % in PAR-char after pre-carbonization and further decreased to 0 wt % after activation (Table 1). This result can also be proved by the XPS result (Figures 4C and 4D). The high-resolution XPS spectra of N 1s were fitted and presented in Figure 4E. The peak at 401.0 eV of PCM_{PAR} and PCM_{PFR+NP} can be ascribed to the binding energy of graphitic-N, whereas the peak at 399.3, 401.0, and 401.9 eV of PCM_{PFR} can be fitted to pyrrolic-N, graphitic-N (eV), and oxided-N, respectively (Sun et al., 2018). The content of the doped-N of all PCMs are around or below 1 atom % (1.14 atom % for PCM_{PAR}, 1.09 atom % for PCM_{PFR}, and 0.60 atom % for PCM_{PFR+NP}). Therefore we concluded that the low content of doped N has little influence on the capacitance performance, which is similar to the effect of phosphorus. X-ray diffraction (XRD) results showed that after PAR pre-carbonization, the nitrogen and phosphorus were transformed to $NH_4H_2PO_4$ in PAR-char. $NH_4H_2PO_4$ may act as an activating agent to create pores.

PCM_{PAR} had fine textural properties with high nitrogen uptakes and a BET surface area of 2,620 $m^2\ g^{-1}$, which was higher than that of PCM_{PFR} (2,233 $m^2\ g^{-1}$). Moreover, PCM_{PAR} had more mesopores than PCM_{PFR}, as proven by the pore size distribution and the average pore diameters (2.3 nm of PCM_{PAR} and 2.1 nm of PCM_{PFR}). To verify the importance of chemically bonded N and P in PAR, equal weight of $NH_4H_2PO_4$ was added in PFR-char for the following activation (PFR-char:$NH_4H_2PO_4$:KOH = 0.59:0.41:4). The results showed that the introduction of $NH_4H_2PO_4$ to the PFR can significantly improve the micropore formation. Thus the pore volume (1.68 $cm^3\ g^{-1}$) and SSA (3,062 $m^2\ g^{-1}$) of PCM_{PFR+NP} increased, which was 1.37 times higher than that of PCM_{PFR} and 1.17 times higher than that of PCM_{PAR}. Therefore both external and *in situ* $NH_4H_2PO_4$ acted as an activating agent to create pores (Li et al., 2010; Xu et al., 2017). However, the *in situ* $NH_4H_2PO_4$ may be helpful in forming mesopores than externally added $NH_4H_2PO_4$. It can be clearly found that PCM_{PAR} has a higher proportion of mesopores/micropores than PCM_{PFR+NP} (Figure 4D). This condition may affect the capacitance performance of PCM.

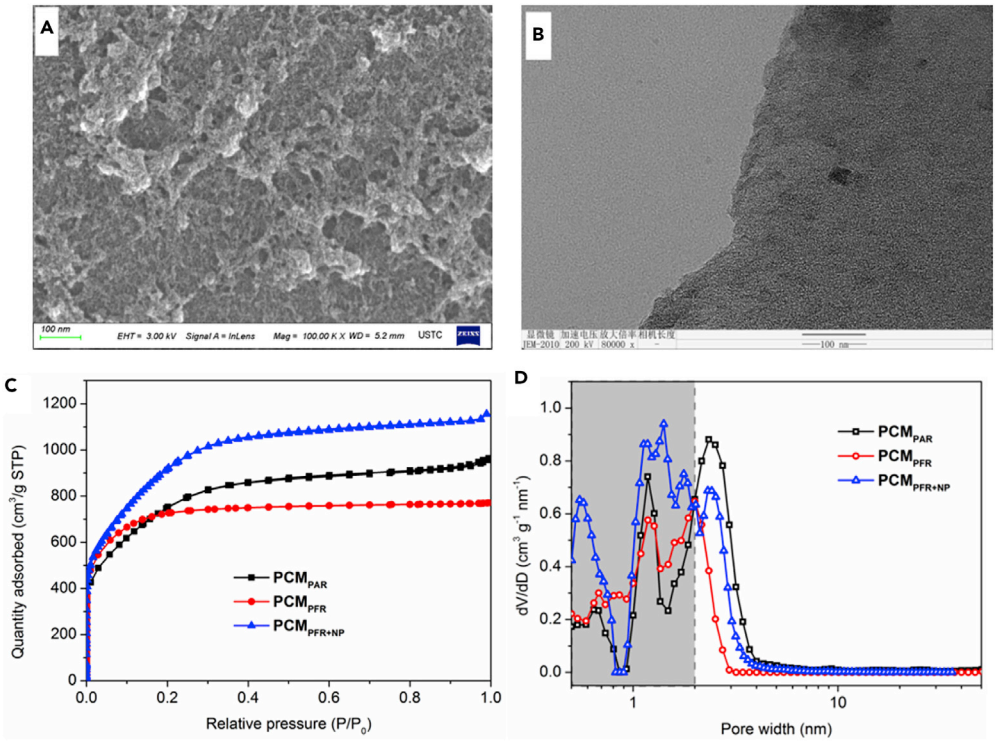

Figure 3. Characterization of the PCMs

(A) SEM image of PCM_{PAR} (scale bar, 100 nm).

(B) TEM image of PCM_{PAR} (scale bar, 100 nm).

(C) N_2 adsorption and desorption isotherms of PCM_{PAR}, PCM_{PFR}, and PCM_{PFR+NP}.

(D) Pore size distributions of PCM_{PAR}, PCM_{PFR}, and PCM_{PFR+NP}.

There are no sharp peaks in the XRD pattern of PCM_{PAR}, PCM_{PFR}, and PCM_{PFR+NP}, indicating the amorphous state of carbon in PCMs (Figure S4). Raman spectra of the PCMs are shown in Figure S5. Two characteristic peaks at 1,340 and 1,580 cm^{-1} are assigned to the defect-induced band (D) and graphitic band (G), respectively (Wang et al., 2018c). The disorder degree of the PCMs can be generally described by the intensity ratio between the D and G bands (I_D/I_G). The I_D/I_G of PCM_{PAR}, PCM_{PFR}, and PCM_{PFR+NP} were 0.90, 0.98, and 0.92, respectively. The slightly lower I_D/I_G of PCM_{PAR} indicated that it had lower disorder degree and higher degree of graphitization, which was beneficial to improve the electric conductivity.

Explanation of the Effect of N and P

The role of N, P in the formation of porous carbon was proposed (Figure 5). In pre-carbonization, N–P and C–N bonds decomposed, and part of the N, P combined with H to form NH_3 and PH_3. The others combined with H and O and transformed to $NH_4H_2PO_4$. The polymer framework was partially carbonized to form a

Sample Code	S_{BET} ($m^2\ g^{-1}$)	V_P[a] ($cm^3\ g^{-1}$)	Pore Size (nm)	Elemental Analysis		XPS Analysis	
				N (wt %)	P (wt %)	N (at%)	P (at%)
PCM_{PAR}	2,620	1.49	2.3	1.07	0	1.14	0.08
PCM_{PFR}	2,233	1.19	2.1	0.80	0	1.09	0
PCM_{PFR+NP}	3,062	1.68	2.2	0.27	0	0.60	0.16

Table 1. Textural and Chemical Properties of PCM_{PAR}, PCM_{PFR}, and PCM_{PFR+NP}

[a]Pore volume determined at $P/P_0 = 0.99$.

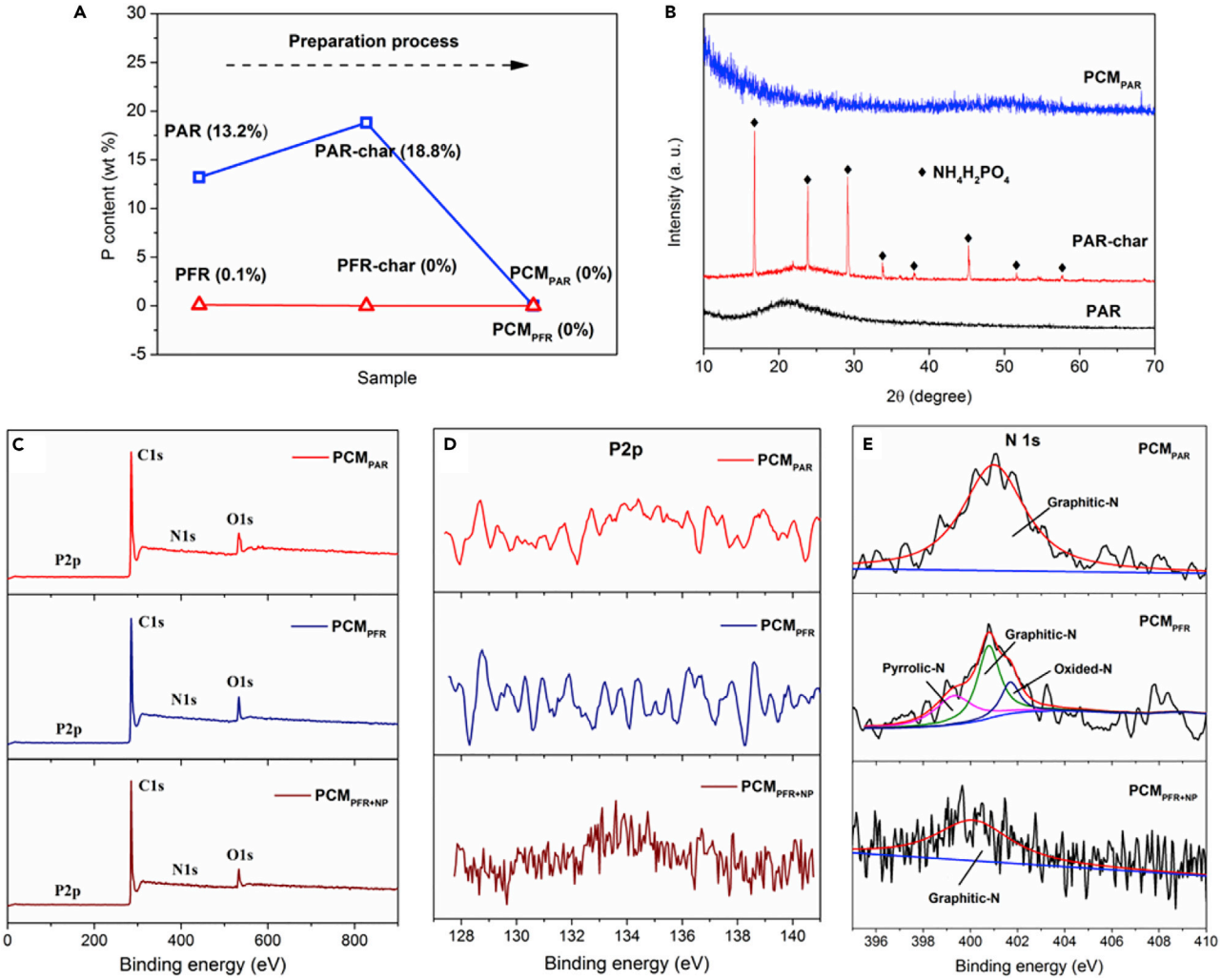

Figure 4. Analysis of Nitrogen and Phosphorus during Thermal Treatment

(A) Transformation of P content during the material preparation.

(B) XRD patterns of PAR and PAR-char.

(C) XPS survey spectra of PCM_{PAR}, PCM_{PFR}, and PCM_{PFR+NP}.

(D) XPS P 2p spectra of PCM_{PAR}, PCM_{PFR}, and PCM_{PFR+NP}.

(E) XPS N 1s spectra of PCM_{PAR}, PCM_{PFR}, and PCM_{PFR+NP}.

$NH_4H_2PO_4$-decorated raw char. During the activation process, KOH could firstly react with the $NH_4H_2PO_4$ as follows: $NH_4H_2PO_4 + 3KOH = NH_3\uparrow + K_3PO_4 + 3H_2O\uparrow$. To confirm this hypothesis, we conducted Thermogravimetric Analysis and Fourier Transform infrared spectroscopy (TG-FTIR) characterizations of PAR samples. The pre-carbonized PAR (PAR-char) and the KOH-added sample (PAR-char + KOH) were first analyzed with a TG analyzer, and the released gaseous products were online analyzed by an FTIR spectrometer. TG-differential thermal gravity (DTG) results show that PAR-char + KOH has a significant weight loss in the range of 100°C –400°C, which is rather different from PAR-char (>600°C). Given that PAR-char was already pre-carbonized at 500°C and exhibited no apparent weight loss (Figure S6), the weight loss of PAR-char + KOH should be caused by the reactions between $NH_4H_2PO_4$ in PAR-char and KOH during carbonization and released gaseous products. Furthermore, FTIR results show that H_2O, NH_3, and CO_2 were the main gaseous products of PAR-char + KOH, whereas little H_2O and NH_3 were released from PAR-char (Figures 5B–5E and S7), demonstrating that the reaction of $NH_4H_2PO_4$ in PAR-char and KOH occurred. Therefore the $NH_4H_2PO_4$ in PAR-char is not easy to decompose below 500°C, but can react with KOH during the heating process. In addition, the main gaseous products (H_2O, NH_3, and CO_2) as well as K_3PO_4 and the excess KOH can all act as activating agents to improve the porosity of

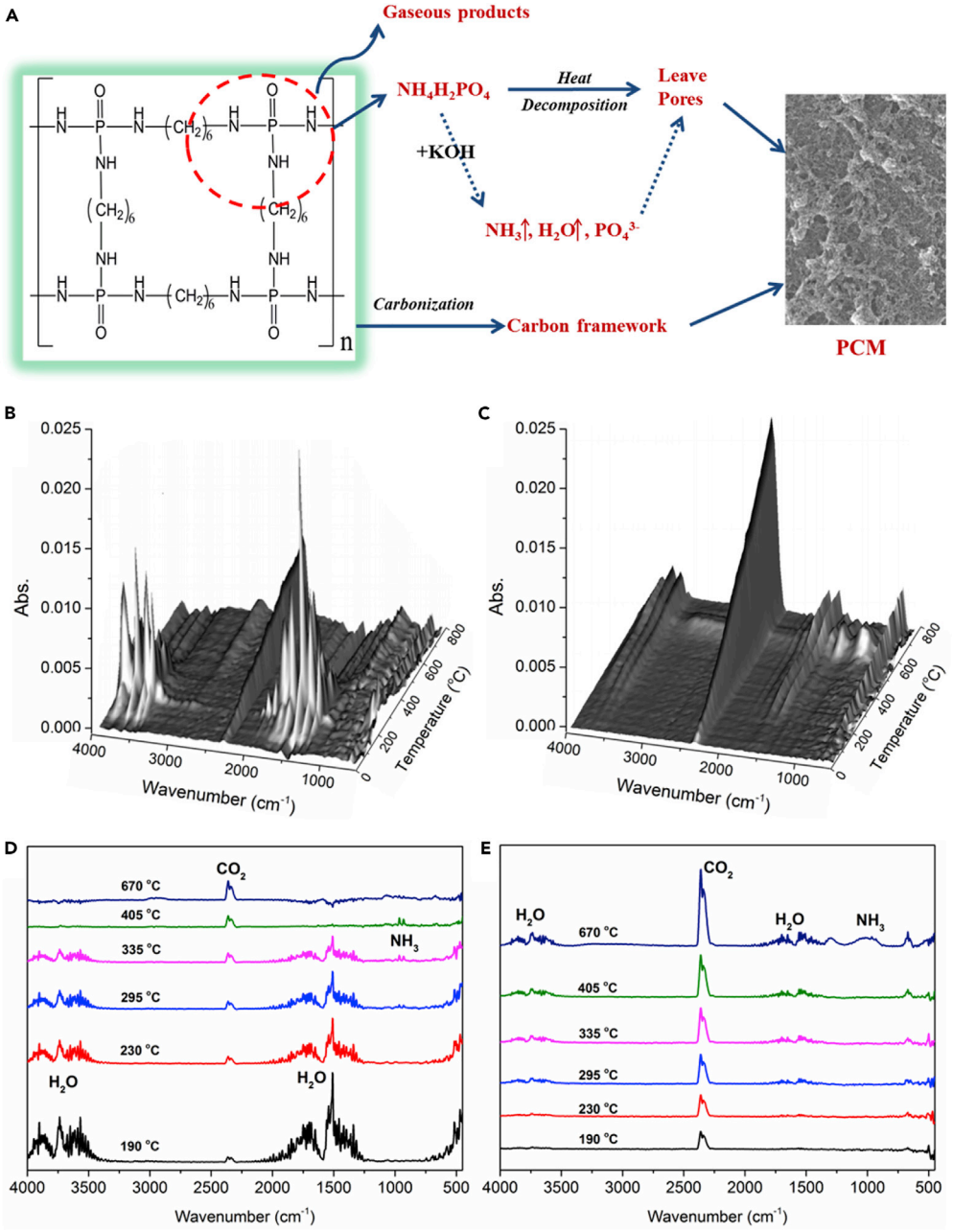

Figure 5. Mechanism of the Formation of Micro/Mesopores

(A) Scheme for PCM_{PAR} synthesis from PAR, and the possible roles played by N and P during the formation of micro/mesopores.

(B) 3D infrared spectrum of gaseous compounds released during pyrolysis of PAR-char + KOH.

(C) 3D infrared spectrum of gaseous compounds released during pyrolysis of PAR-char.

(D) FTIR spectra of pyrolysis products of PAR-char + KOH at selected temperatures.

(E) FTIR spectra of pyrolysis products of PAR-char at selected temperatures.

carbon substrate. Besides, the pre-carbonized PAR was just physically mixed with KOH powder, thus the $NH_4H_2PO_4$ embedded in carbon was partially in contact with KOH. Importantly, the special N–P structure of PAR formed highly dispersed $NH_4H_2PO_4$ and thus resulted in the development of well-distributed micro/mesopores, which is beneficial to improve the capacitance performance (Li et al., 2014; Zheng et al., 2015).

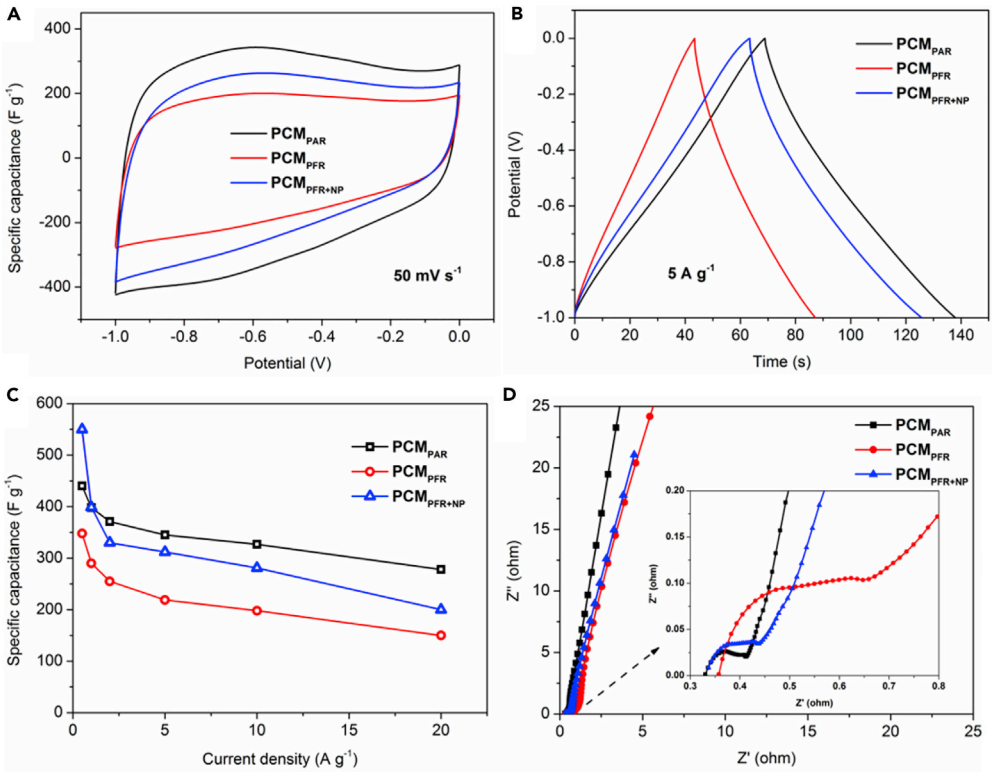

Figure 6. Electrochemical Characterization of the PCMs in Three-Electrode System

(A) CV curves of the PCMs at scan rate of 50 mV s^{-1}.

(B) GCD profiles of the PCMs under current density of 5 A g^{-1}.

(C) Specific capacitance of the PCMs calculated by GCD profiles.

(D) EIS plots of the PCMs.

Electrochemical Performance of the PCMs

The electrochemical performance of the PCMs was investigated with CV and GCD measurements. The cyclic voltammetry (CV) curves and galvanostatical charge–discharge (GCD) profiles of PCMs are shown in Figure S8. The CV curves of PCM_{PAR} under wide scan rates from 5 mV s^{-1} to 100 mV s^{-1} showed a similarly rectangular and symmetric shape (Figure S8A). Importantly, the CV curves of PCM_{PAR} still maintained a rectangular shape even at a sweep rate of 100 mV s^{-1} and an inapparent reduction in the CV area. This phenomenon indicated that PCM_{PAR} has a fine ion transporting and accessible surface area. The PCM_{PFR} and PCM_{PFR+NP} had similar CV shapes with PCM_{PAR} but suffered an area distortion at a high scan rate and a prominent area reduction with the increase in scan rate. This condition indicated a poor capacitance performance of PCM_{PFR} and PCM_{PFR+NP} at high charge-discharge rate. Instead of the typical rectangular shape, a region of reversible pseudofaradaic reaction can be observed at about −0.5 V in the CV curves. In addition, the approximate triangular charge-discharge profiles and their slightly nonlinear characteristic exhibited the primary EDLC performance and additional pseudocapacitance performance (Figure S8B). The pseudocapacitance can be attributed to the high oxygen content (7%–8%) of the PCMs (Table S1) (Guo et al., 2014; Liu et al., 2018; Tang et al., 2017).

CV curves of the PCMs at scan rate of 50 mV s^{-1} show that the specific capacitance has an order of PCM_{PAR}>PCM_{PFR+NP}>PCM_{PFR} (Figure 6A). The result can also be proved by the GCD profiles under current density of 5 A g^{-1} (Figure 6B). The GCD measurements were performed under different current densities to assess specific capacitance (Figure 6C). The PCM_{PAR} showed a high specific capacitance of 440 F g^{-1} under a current density of 0.5 A g^{-1} and still maintained at 278 F g^{-1} at a high current density of 20 A g^{-1}. This PCM material shows a competitive performance among carbon-based supercapacitor electrodes (Table S2). As a comparison, the specific capacitances of PCM_{PFR} and PCM_{PFR+NP} are also listed in Figure 6C. PCM_{PFR} had the lowest specific capacitance (348 F g^{-1} at 0.5 A g^{-1} and 150 F g^{-1}

at 20 A g^{-1}) attributed to the lowest SSA (2,233 m^2 g^{-1}) because the specific capacitance of EDLC mainly depended on the SSA and porosity characteristics of electrode materials. PCM_{PFR+NP} (3,062 m^2 g^{-1}) had larger SSA than PCM_{PAR} (2,620 m^2 g^{-1}), but the specific capacitance of PCM_{PFR+NP} was not higher than that of PCM_{PAR} under overall current densities. When the current density was below 1 A g^{-1}, PCM_{PFR+NP} exhibited higher specific capacitance than PCM_{PAR}. However, when the current density was above 1 A g^{-1}, PCM_{PAR} showed high specific capacitance. At low charge-discharge rate, ions from the electrolyte had enough time to accumulate on the electrode surface. Therefore, SSA dominated the capacitance performance. Meanwhile, at high charge-discharge rate, ions cannot be delivered to the surface in time owing to the limitation of the pore structure. This phenomenon indicated that SSA was not finely utilized. As a result, the pore characteristics and the accessible surface area determined the specific capacitance at high charge-discharge rate. Researchers found hierarchical porous microstructures, namely, proper macroporous, mesoporous, and microporous distributions, which are favorable for the diffusion of electrolyte ions, thus leading to a high-rate electrochemical capacitance (Li et al., 2013; Zhang et al., 2016; Zheng et al., 2010). The pore size distribution showed that PCM_{PAR} has more mesopores than PCM_{PFR} and PCM_{PFR+NP} (Figure 2D). With the increase of the proportion of mesopores, PCM_{PAR} can provide a sufficient electrode-electrolyte interface for the accumulation of ions. Thus capacitance performance was improved.

Electrochemical impedance spectroscopy (EIS) was performed to further understand the ion or charge transport of the PCMs. As shown in Figure 6D, in the low-frequency region, the PCMs showed almost vertical curves, wherein PCM_{PAR} had the highest slope. This phenomenon indicated the nearly ideal EDLC behavior and the small equivalent diffusion resistance. In the high-frequency region (inset in Figure 6D), the intercept on the real axis presented low values (<0.4 Ω). This finding corresponded to low equivalent series resistances and indicated the excellent conductivity of the PCMs in aqueous electrolyte system. From the high- to low-frequency region, the low interfacial charge transfer resistances calculated from the diameter of the semicircle were 0.09 Ω of PCM_{PAR}, 0.29 Ω of PCM_{PFR}, and 0.10 Ω of PCM_{PFR+NP}. The EIS results showed that PCM_{PAR} had smaller contact resistance among the electrode materials and electrolyte ions, indicating lower charge transfer resistance on the electrode surface. Furthermore, the cycling stability of the PCM_{PAR} was evaluated by long-term CV cycling measurement at a scan rate of 50 mV s^{-1}. The result showed that PCM_{PAR} has fine capacitance retention of 93% over 10,000 cycles (Figure S9). Besides, PCM_{PAR}, PCM_{PFR}, and PCM_{PFR+NP} are all soaked well in water (Figure S10 and Table S3), which has no negative effect when used as electrode materials in aqueous solution. Combining the results of CV, GCD, EIS, and long-term cycling, PCM_{PAR} exhibited a favorable performance as supercapacitor electrode.

Electrochemical Tests in Two-Electrode System

The electrochemical performance of PCM_{PAR} in a two-electrode system is shown in Figure S8. The PCM_{PAR} showed similar rectangular CV curves as well as approximate triangular GCD profiles (Figures 7A and 7B), indicative of a primary EDLC performance. The specific capacitances of PCM_{PAR} calculated by GCD profiles were 279, 255, 237, 210, 191, and 174 F g^{-1} at current densities of 0.5, 1, 2, 5, 10, and 20 A g^{-1}, respectively (Figure 7C). These values were competitive during the carbon materials. Furthermore, the energy density and power density were calculated, and the results are shown in Figure 7D. PCM_{PAR} exhibited an energy density of 9.7 Wh kg^{-1} or 6.0 Wh kg^{-1}. This value corresponded to a power density of 0.25 kW kg^{-1} or 10 kW kg^{-1} in 6 M KOH electrolyte.

DISCUSSION

Phosphoramide resin was synthesized, wherein the special N–P structure was chemically bonded as the nodes for linking the monomers into polymers. The N and P in the PAR framework can be transformed to $NH_4H_2PO_4$ during carbonization. The well-distributed $NH_4H_2PO_4$ acts as the *in situ* activating agent to form micro/mesopores, which has better effect on activation than post-added $NH_4H_2PO_4$. The as-prepared PCM_{PAR} has a high SSA of 2,620 m^2 g^{-1} and pore volume of 1.49 cm^3 g^{-1} and fine micro/mesoporous structure. Electrochemical tests show that PCM_{PAR} has approximately rectangular CV curves and triangular GCD profiles. This finding indicates that PCM_{PAR} is a typical EDLC electrode. The PCM_{PAR} exhibits a specific capacitance of 440 F g^{-1} at 0.5 A g^{-1} and 278 F g^{-1} at 20 A g^{-1}. The high capacitance retention at high charge-discharge rates signifies that PCM_{PAR} has fine micro/mesoporous structure for the transport of electrolyte ions. The results show that PAR is a good candidate to prepare PCMs for supercapacitor because of its unique form of N and P in the framework.

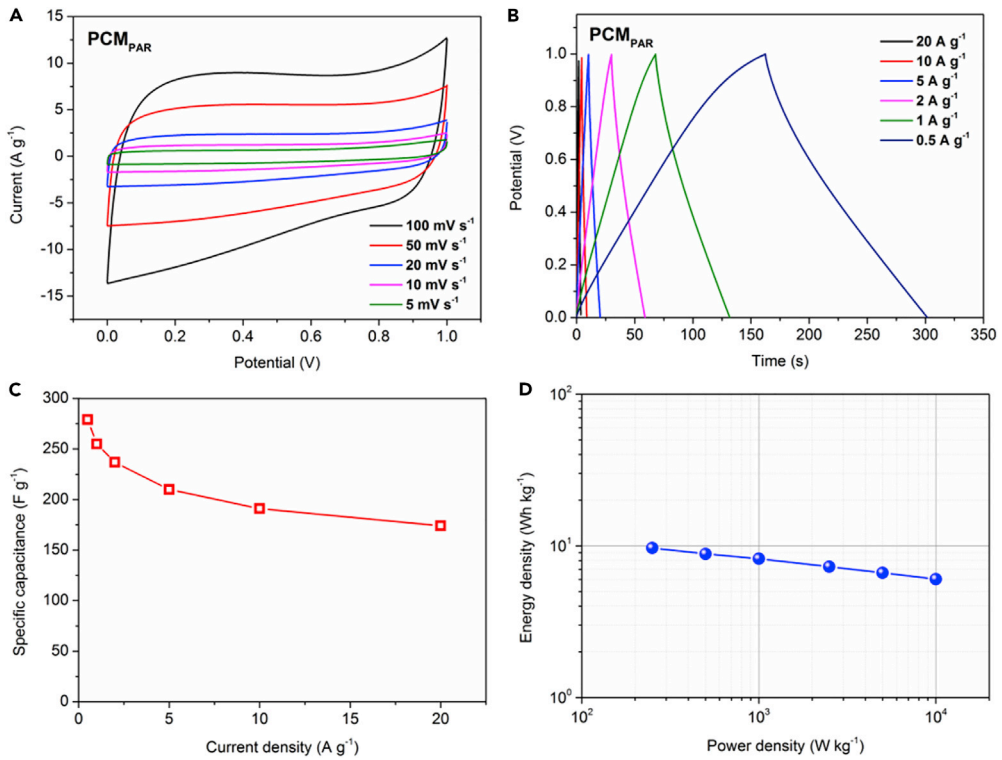

Figure 7. Electrochemical Characterization of the PCM$_{PAR}$ in Two-Electrode System

(A) CV curves of PCM$_{PAR}$ at different scan rates in a two-electrode system.

(B) GCD profiles of PCM$_{PAR}$ under different current densities.

(C) Specific capacitance of PCM$_{PAR}$ calculated by GCD profiles.

(D) Ragone plot of PCM$_{PAR}$.

Limitations of Study

Based on the current preparation method of PCMs from PAR involving drastic activation, it is hard to precisely control the pore size. Therefore we would design and synthesize more N, P resins by changing the monomers in future work and adopt the mild activation process. The effect of monomer structures on the characteristics of the PCMs should be investigated to optimize the design and preparation of new PCMs for energy storage, catalysis, environmental remediation, and so on.

METHODS

All methods can be found in the accompanying Transparent Methods supplemental file.

SUPPLEMENTAL INFORMATION

Supplemental Information includes Transparent Methods, 10 figures, 3 tables, and 2 data files and can be found with this article online at https://doi.org/10.1016/j.isci.2019.01.016.

ACKNOWLEDGMENTS

The authors gratefully acknowledge financial support from National Natural Science Foundation of China (21677138) and the Key Special Program on the S&T for the Pollution Control and Treatment of Water Bodies (No. 2017ZX07603-003 and No.2012ZX07103−001).

AUTHOR CONTRIBUTIONS

H.J. developed the concept, designed the experiment, analyzed the data, and composed the manuscript. B.-H.C carried out the experiments and wrote the article. R.J. Z. coordinated the project. All authors provided critical discussion of the data and ideas and gave input on the manuscript.

DECLARATION OF INTERESTS

The authors declare no competing interests.

Received: September 7, 2018
Revised: December 21, 2018
Accepted: January 8, 2019
Published: February 22, 2019

REFERENCES

Böttger-Hiller, F., Kempe, P., Cox, G., Panchenko, A., Janssen, N., Petzold, A., Thurn-Albrecht, T., Borchardt, L., Rose, M., Kaskel, S., et al. (2013). Twin polymerization at spherical hard templates: an approach to size-adjustable carbon hollow spheres with micro- or mesoporous shells. Angew. Chem. Int. Ed. *52*, 6088–6091.

Chmiola, J., Yushin, G., Dash, R., and Gogotsi, Y. (2006a). Effect of pore size and surface area of carbide derived carbons on specific capacitance. J. Power Sources *158*, 765–772.

Chmiola, J., Yushin, G., Gogotsi, Y., Portet, C., Simon, P., and Taberna, P.L. (2006b). Anomalous increase in carbon capacitance at pore sizes less than 1 nanometer. Science *313*, 1760–1763.

Chuenchom, L., Kraehnert, R., and Smarsly, B.M. (2012). Recent progress in soft-templating of porous carbon materials. Soft Matter *8*, 10801–10812.

Dutta, S., Bhaumik, A., and Wu, K.C.W. (2014). Hierarchically porous carbon derived from polymers and biomass: effect of interconnected pores on energy applications. Energy Environ. Sci. *7*, 3574–3592.

Estevez, L., Dua, R., Bhandari, N., Ramanujapuram, A., Wang, P., and Giannelis, E.P. (2013). A facile approach for the synthesis of monolithic hierarchical porous carbons - high performance materials for amine based CO2 capture and supercapacitor electrode. Energy Environ. Sci. *6*, 1785–1790.

Guo, C., Li, N., Ji, L., Li, Y., Yang, X., Lu, Y., and Tu, Y. (2014). N- and O-doped carbonaceous nanotubes from polypyrrole for potential application in high-performance capacitance. J. Power Sources *247*, 660–666.

Hasegawa, G., Kanamori, K., Kiyomura, T., Kurata, H., Abe, T., and Nakanishi, K. (2016). Hierarchically porous carbon monoliths comprising ordered mesoporous nanorod assemblies for high-voltage aqueous supercapacitors. Chem. Mater. *28*, 3944–3950.

Hou, J., Cao, C., Idrees, F., and Ma, X. (2015). Hierarchical porous nitrogen-doped carbon nanosheets derived from silk for ultrahigh-capacity battery anodes and supercapacitors. ACS Nano *9*, 2556–2564.

Hu, J., Wang, H., Gao, Q., and Guo, H. (2010). Porous carbons prepared by using metal–organic framework as the precursor for supercapacitors. Carbon *48*, 3599–3606.

Hu, M., Reboul, J., Furukawa, S., Torad, N.L., Ji, Q., Srinivasu, P., Ariga, K., Kitagawa, S., and Yamauchi, Y. (2012). Direct carbonization of Al-based porous coordination polymer for synthesis of nanoporous carbon. J. Am. Chem. Soc. *134*, 2864–2867.

Huang, Y.-B., Pachfule, P., Sun, J.-K., and Xu, Q. (2016). From covalent-organic frameworks to hierarchically porous B-doped carbons: a molten-salt approach. J. Mater. Chem. A *4*, 4273–4279.

Kondrat, S., Perez, C.R., Presser, V., Gogotsi, Y., and Kornyshev, A.A. (2012). Effect of pore size and its dispersity on the energy storage in nanoporous supercapacitors. Energy Environ. Sci. *5*, 6474–6479.

Krüner, B., Schreiber, A., Tolosa, A., Quade, A., Badaczewski, F., Pfaff, T., Smarsly, B.M., and Presser, V. (2018). Nitrogen-containing novolac-derived carbon beads as electrode material for supercapacitors. Carbon *132*, 220–231.

Largeot, C., Portet, C., Chmiola, J., Taberna, P.-L., Gogotsi, Y., and Simon, P. (2008). Relation between the ion size and pore size for an electric double-layer capacitor. J. Am. Chem. Soc. *130*, 2730–2731.

Li, K., Li, Y., and Zheng, Z. (2010). Kinetics and mechanism studies of p-nitroaniline adsorption on activated carbon fibers prepared from cotton stalk by NH4H2PO4 activation and subsequent gasification with steam. J. Hazard. Mater. *178*, 553–559.

Li, Y., Li, Z., and Shen, P.K. (2013). Simultaneous formation of ultrahigh surface area and three-dimensional hierarchical porous graphene-like networks for fast and highly stable supercapacitors. Adv. Mater. *25*, 2474–2480.

Li, Z., Wu, D., Liang, Y., Fu, R., and Matyjaszewski, K. (2014). Synthesis of well-defined microporous carbons by molecular-scale templating with polyhedral oligomeric silsesquioxane moieties. J. Am. Chem. Soc. *136*, 4805–4808.

Liang, C., and Dai, S. (2006). Synthesis of mesoporous carbon materials via enhanced hydrogen-bonding interaction. J. Am. Chem. Soc. *128*, 5316–5317.

Liu, T., Zhang, F., Song, Y., and Li, Y. (2017). Revitalizing carbon supercapacitor electrodes with hierarchical porous structures. J. Mater. Chem. A *5*, 17705–17733.

Liu, W., Zhang, S., Dar, S.U., Zhao, Y., Akram, R., Zhang, X., Jin, S., Wu, Z., and Wu, D. (2018). Polyphosphazene-derived heteroatoms-doped carbon materials for supercapacitor electrodes. Carbon *129*, 420–427.

Pandolfo, A.G., and Hollenkamp, A.F. (2006). Carbon properties and their role in supercapacitors. J. Power Sources *157*, 11–27.

Puthusseri, D., Aravindan, V., Madhavi, S., and Ogale, S. (2014). 3D micro-porous conducting carbon beehive by single step polymer carbonization for high performance supercapacitors: the magic of in situ porogen formation. Energy Environ. Sci. *7*, 728–735.

Qie, L., Chen, W., Xu, H., Xiong, X., Jiang, Y., Zou, F., Hu, X., Xin, Y., Zhang, Z., and Huang, Y. (2013). Synthesis of functionalized 3D hierarchical porous carbon for high-performance supercapacitors. Energy Environ. Sci. *6*, 2497–2504.

Salanne, M., Rotenberg, B., Naoi, K., Kaneko, K., Taberna, P.L., Grey, C.P., Dunn, B., and Simon, P. (2016). Efficient storage mechanisms for building better supercapacitors. Nat. Energy *1*, 16070.

Sevilla, M., and Fuertes, A.B. (2014). Direct synthesis of highly porous interconnected carbon nanosheets and their application as high-performance supercapacitors. ACS Nano *8*, 5069–5078.

Simon, P., and Gogotsi, Y. (2008). Materials for electrochemical capacitors. Nat. Mater. *7*, 845–854.

Strauss, V., Marsh, K., Kowal, M.D., El-Kady, M., and Kaner, R.B. (2018). A simple route to porous graphene from carbon nanodots for supercapacitor applications. Adv. Mater. *30*, 1704449.

Su, Y.-Z., Xiao, K., Li, N., Liu, Z.-Q., and Qiao, S.-Z. (2014). Amorphous Ni(OH)2 @ three-dimensional Ni core–shell nanostructures for high capacitance pseudocapacitors and asymmetric supercapacitors. J. Mater. Chem. A *2*, 13845–13853.

Sun, H., Wang, J.-G., Zhang, Y., Hua, W., Li, Y., and Liu, H. (2018). Ultrafast lithium energy storage enabled by interfacial construction of interlayer-expanded MoS2/N-doped carbon nanowires. J. Mater. Chem. A *6*, 13419–13427.

Tang, C., Liu, Y., Yang, D., Yang, M., and Li, H. (2017). Oxygen and nitrogen co-doped porous carbons with finely-layered schistose structure for high-rate-performance supercapacitors. Carbon *122*, 538–546.

Tao, Y., Kanoh, H., Abrams, L., and Kaneko, K. (2006). Mesopore-modified zeolites: preparation, characterization, and applications. Chem. Rev. *106*, 896–910.

Tian, W., Gao, Q., Tan, Y., Yang, K., Zhu, L., Yang, C., and Zhang, H. (2015). Bio-inspired beehive-like hierarchical nanoporous carbon derived from bamboo-based industrial by-product as a high performance supercapacitor electrode material. J. Mater. Chem. A *3*, 5656–5664.

Tran, C., and Kalra, V. (2013). Fabrication of porous carbon nanofibers with adjustable pore sizes as electrodes for supercapacitors. J. Power Sources *235*, 289–296.

Wang, G., Zhang, L., and Zhang, J. (2012). A review of electrode materials for electrochemical supercapacitors. Chem. Soc. Rev. *41*, 797–828.

Wang, J.-G., Kang, F., and Wei, B. (2015). Engineering of MnO2-based nanocomposites for high-performance supercapacitors. Prog. Mater. Sci. *74*, 51–124.

Wang, J.-G., Liu, H., Liu, H., Hua, W., and Shao, M. (2018a). Interfacial constructing flexible V2O5@polypyrrole core–shell nanowire membrane with superior supercapacitive performance. ACS Appl. Mater. Interfaces *10*, 18816–18823.

Wang, J.-G., Liu, H., Sun, H., Hua, W., Wang, H., Liu, X., and Wei, B. (2018b). One-pot synthesis of nitrogen-doped ordered mesoporous carbon spheres for high-rate and long-cycle life supercapacitors. Carbon *127*, 85–92.

Wang, J.-G., Sun, H., Liu, H., Jin, D., Liu, X., Li, X., and Kang, F. (2018c). Triaxialnanocables of conducting polypyrrole@SnS2@carbon nanofiber enabling significantly enhanced Li-Ion storage. ACS Appl. Mater. Interfaces *10*, 13581–13587.

Wang, J., and Kaskel, S. (2012). KOH activation of carbon-based materials for energy storage. J. Mater. Chem. *22*, 23710–23725.

Wei, J., Zhou, D., Sun, Z., Deng, Y., Xia, Y., and Zhao, D. (2013). A controllable synthesis of rich nitrogen-doped ordered mesoporous carbon for CO2 capture and supercapacitors. Adv. Funct. Mater. *23*, 2322–2328.

Xiong, S., Fan, J., Wang, Y., Zhu, J., Yu, J., and Hu, Z. (2017). A facile template approach to nitrogen-doped hierarchical porous carbon nanospheres from polydopamine for high-performance supercapacitors. J. Mater. Chem. A *5*, 18242–18252.

Xu, B., Zheng, D., Jia, M., Cao, G., and Yang, Y. (2013). Nitrogen-doped porous carbon simply prepared by pyrolyzing a nitrogen-containing organic salt for supercapacitors. Electrochim. Acta *98*, 176–182.

Xu, D., Tong, Y., Yan, T., Shi, L., and Zhang, D. (2017). N,P-codopedmeso-/microporous carbon derived from biomass materials via a dual-activation strategy as high-performance electrodes for deionization capacitors. ACS Sustain. Chem. Eng. *5*, 5810–5819.

Yao, L., Wu, Q., Zhang, P., Zhang, J., Wang, D., Li, Y., Ren, X., Mi, H., Deng, L., and Zheng, Z. (2018). Scalable 2D hierarchical porous carbon nanosheets for flexible supercapacitors with ultrahigh energy density. Adv. Mater. *30*, 1706054.

Yu, D., Goh, K., Wang, H., Wei, L., Jiang, W., Zhang, Q., Dai, L., and Chen, Y. (2014). Scalable synthesis of hierarchically structured carbon nanotube–graphene fibres for capacitive energy storage. Nat. Nanotechnol. *9*, 555.

Zeng, F.-X., Liu, W.-J., Luo, S.-W., Jiang, H., Yu, H.-Q., and Guo, Q.-X. (2011). Design, preparation, and characterization of a novel hyper-cross-linked polyphosphamide polymer and its adsorption for phenol. Ind. Eng. Chem. Res. *50*, 11614–11619.

Zhai, Y., Dou, Y., Zhao, D., Fulvio, P.F., Mayes, R.T., and Dai, S. (2011). Carbon materials for chemical capacitive energy storage. Adv. Mater. *23*, 4828–4850.

Zhang, L., Jiang, Y., Wang, L., Zhang, C., and Liu, S. (2016). Hierarchical porous carbon nanofibers as binder-free electrode for high-performance supercapacitor. Electrochim. Acta *196*, 189–196.

Zhang, L.L., and Zhao, X.S. (2009). Carbon-based materials as supercapacitor electrodes. Chem. Soc. Rev. *38*, 2520–2531.

Zhang, P., Yuan, J., Fellinger, T.-P., Antonietti, M., Li, H., and Wang, Y. (2013). Improving hydrothermal carbonization by using poly(ionic liquid)s. Angew. Chem. Int. Ed. *52*, 6028–6032.

Zheng, C., Qi, L., Yoshio, M., and Wang, H. (2010). Cooperation of micro- and meso-porous carbon electrode materials in electric double-layer capacitors. J. Power Sources *195*, 4406–4409.

Zheng, X., Luo, J., Lv, W., Wang, D.-W., and Yang, Q.-H. (2015). Two-dimensional porous carbon: synthesis and ion-transport properties. Adv. Mater. *27*, 5388–5395.

Zhong, M., Kim, E.K., McGann, J.P., Chun, S.-E., Whitacre, J.F., Jaroniec, M., Matyjaszewski, K., and Kowalewski, T. (2012). Electrochemically active nitrogen-enriched nanocarbons with well-defined morphology synthesized by pyrolysis of self-assembled block copolymer. J. Am. Chem. Soc. *134*, 14846–14857.

Zhou, J., Zhu, T., Xing, W., Li, Z., Shen, H., and Zhuo, S. (2015). Activated polyaniline-based carbon nanoparticles for high performance supercapacitors. Electrochim. Acta *160*, 152–159.

Zhu, D., Wang, Y., Gan, L., Liu, M., Cheng, K., Zhao, Y., Deng, X., and Sun, D. (2015). Nitrogen-containing carbon microspheres for supercapacitor electrodes. Electrochim. Acta *158*, 166–174.

ISCI, Volume *12*

Supplemental Information

Nontemplating Porous Carbon Material from Polyphosphamide Resin for Supercapacitors

Bin-Hai Cheng, Fan-Xin Zeng, Wen-Jing Chen, Hui-Yuan Cheng, Raymond J. Zeng, and Hong Jiang

Supporting Information

Nontemplating porous carbon material from polyphosphamide resin for supercapacitors

Bin-Hai Cheng[a,b], Fan-Xin Zeng[b], Wen-Jing Chen[b], Hui-Yuan Cheng[b], Raymond J. Zeng[a,b], Hong Jiang[b,*]

[a] School of Life sciences, University of Science and Technology of China

[b] Biomass Clean Energy Laboratory, Department of Chemistry, University of Science and Technology of China

Corresponding author:

Dr. Hong Jiang, Fax: +86-551-63607482; E-mail: jhong@ustc.edu.cn

Table S1. Oxygen content of PCM_{PAR}, PCM_{PFR}, and PCM_{PFR+NP}, Related to Figure 6

Sample code	Elemental analysis	XPS analysis
	O (wt%)	O (at%)
PCM_{PAR}	8.20	9.84
PCM_{PFR}	7.86	7.55
PCM_{PFR+NP}	7.32	9.49

Table S2. Comparison of specific capacitance between the PCM_{PAR} and other carbon materials, Related to Figure 6

Supercapacitor materials	Specific surface area ($m^2 g^{-1}$)	Max. capacitance ($F g^{-1}$)	Scan rate or current density	Electrolyte	Cycle number	Stability	Ref.
Hierarchical porous carbon	1593	298	1 mV s^{-1}	1 M H_2SO_4	5,000	96.7%	(Zhang et al., 2018)
N,P,S-codoped hierarchically porous carbon spheres	1258	274	0.5 A g^{-1}	6 M KOH	10,000	95%	(Yan et al., 2018)
Hierarchically porous carbon nanotubes	1419	286	0.1 A g^{-1}	6 M KOH	10,000	~100%	(Wang et al., 2018a)
N/S-co-doped carbon nanobowls	1567	279	0.1 A g^{-1}	6 M KOH	50,000	90.8%	(Wang et al., 2018b)
hollow particle-based N-doped carbon nanofibers	418	307	1.0 A g^{-1}	2 M H_2SO_4	10,000	98.2%	(Chen et al., 2017)
Ultrathin porous carbon shell	662	251	1.0 A g^{-1}	6 M KOH	10,000	97%	(Yang et al., 2017)
N-doped carbon with pillared-layered pores	2118	305	0.2 A g^{-1}	6 M NaOH	10,000	89.1%	(Tian et al., 2017)
Phosphorus-doped 3D hierarchical porous carbon	940	367	0.3 A g^{-1}	6 M KOH	10,000	96.5%	(Yang et al., 2018)
Hierarchically porous nitrogen-doped carbon	2905	302	1.0 A g^{-1}	6 M KOH	10,000	95%	(Zou et al., 2018)
Two dimensional holey carbon nanosheets	1258	360	1.0 A g^{-1}	6 M KOH	10,000	97.7%	(Cai et al., 2018)
P,N,O co-doped polymer-based core-shell carbon sphere	595	157	0.05 A g^{-1}	1 M H_2SO_4	10,000	85%	(Huang et al., 2018)
N,S self-doped porous carbon nanosheets	986	280	1.0 A g^{-1}	6 M KOH	10,000	94.4%	(Miao et al., 2018)

PCM_{PAR}	**2620**	**440**	**0.5 A g^{-1}**	**6 M KOH**	**10, 000**	**93%**	**This work**

Table S3. Oxygen content of PCM_{PAR} and PCM_{PFR} before and after 10,000 cycles, Related to Figure 6

	original	**after 10,000 cycles**
PCM_{PAR}	9.84 at%	14.86 at%
PCM_{PFR}	7.55 at%	19.09 at%

Both the oxygen contents of PCM_{PAR} and PCM_{PFR} are increased after 10,000 cycles from the results of XPS survey (Table S2), indicating that the surface of the materials is oxidized to different extent.

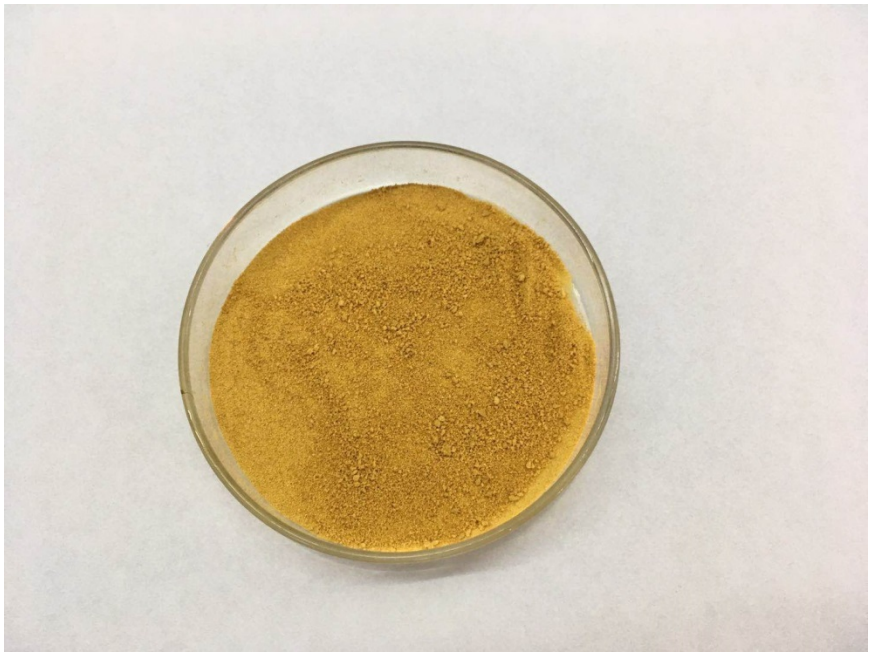

Figure S1. Photograph of the as-synthesized PAR, Related to Scheme 1

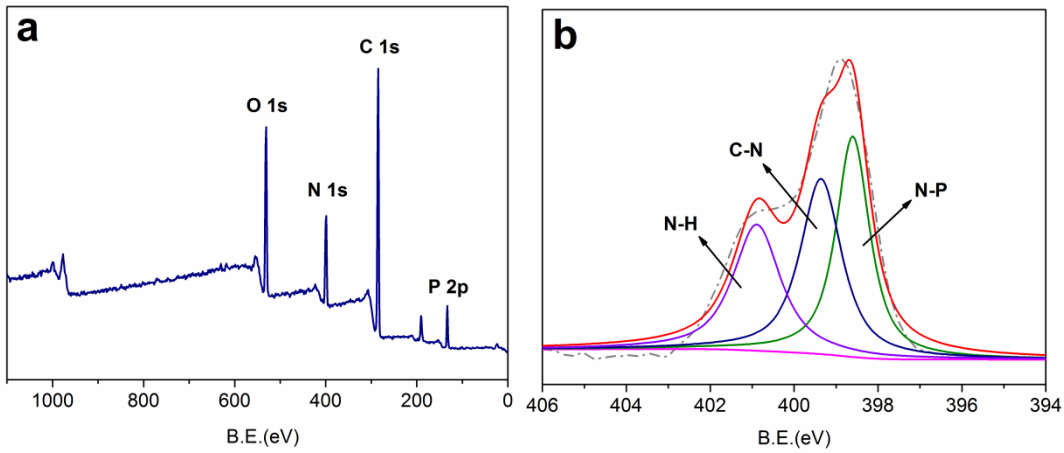

Figure S2. XPS spectra of PAR, Related to Figure 2

(a) XPS survey spectrum of PAR.

(b) XPS N 1s spectrum of PAR.

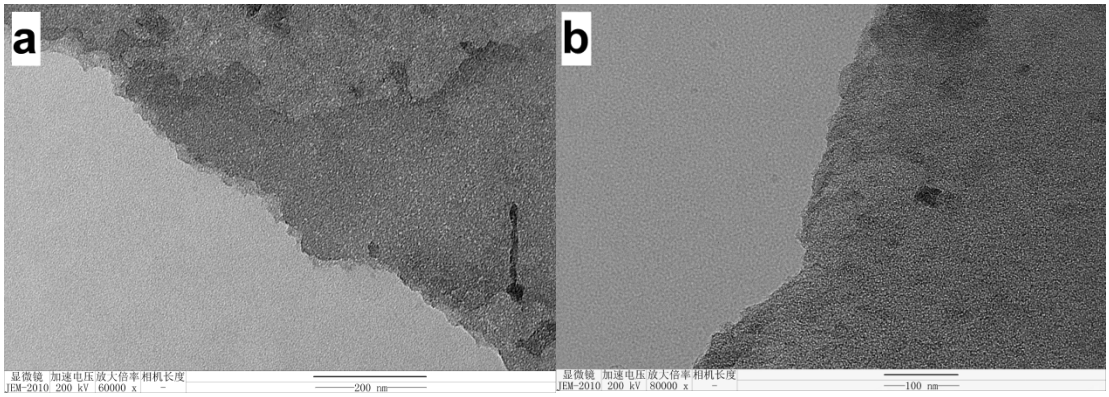

Figure S3. TEM images of PCM_{PAR}, Related to Figure 3

(a) A scale bar of 200 nm.

(b) A scale bar of 100 nm.

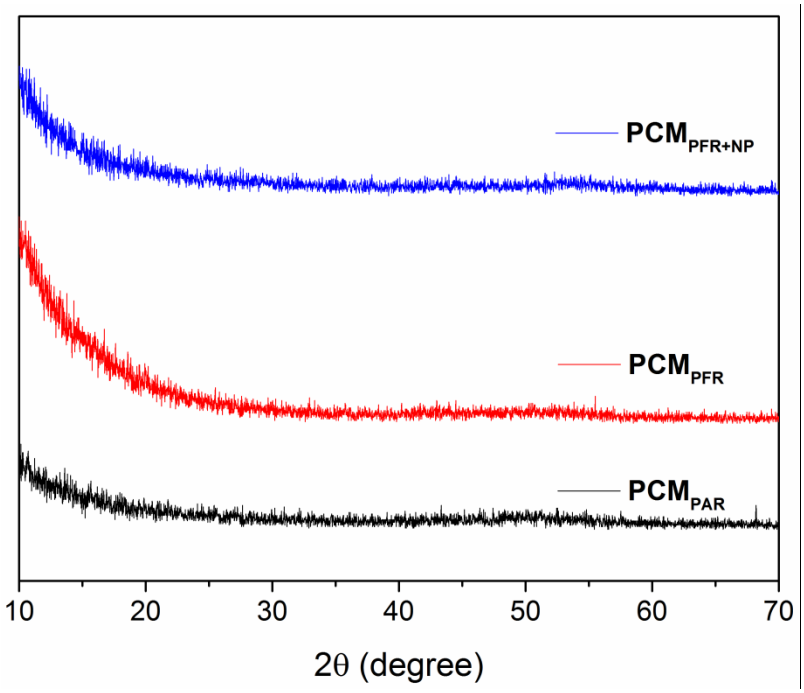

Figure S4. XRD patterns of PCM_{PAR}, PCM_{PFR}, and PCM_{PFR+NP}, Related to Figure3

As shown in Fig. S4, no sharp peaks are observed in the XRD pattern, indicative of the amorphous state of carbon in PCMs.

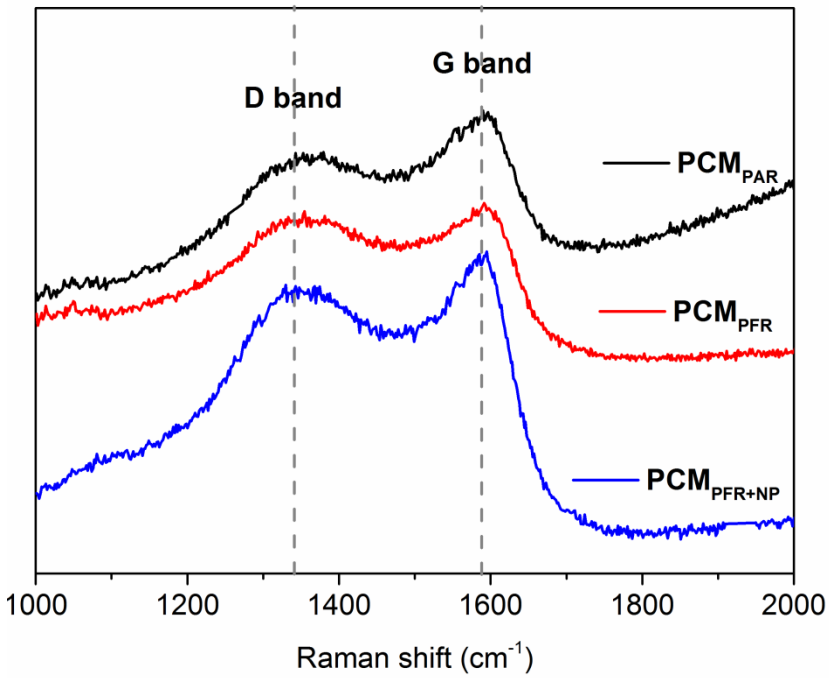

Figure S5. Raman spectra of PCM_{PAR}, PCM_{PFR}, and PCM_{PFR+NP}, Related to Figure 3

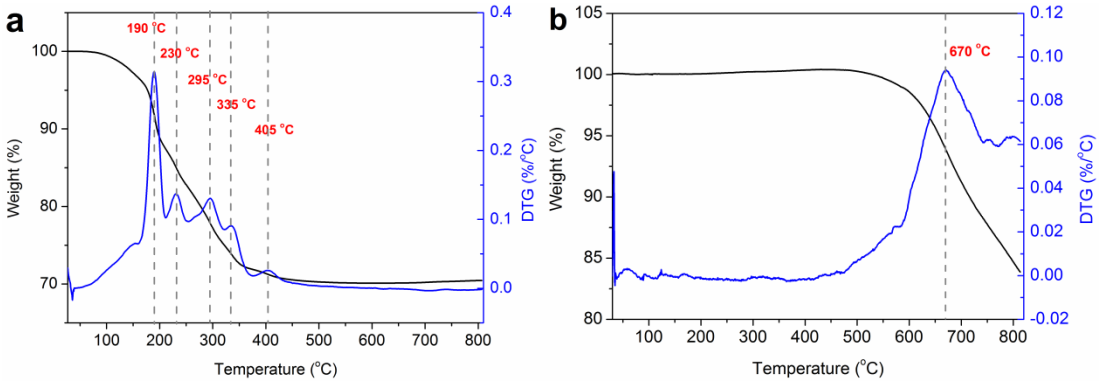

Figure S6. TG-DTG curves, Related to Figure 5

(a) PAR-char+KOH.

(b) PAR-char.

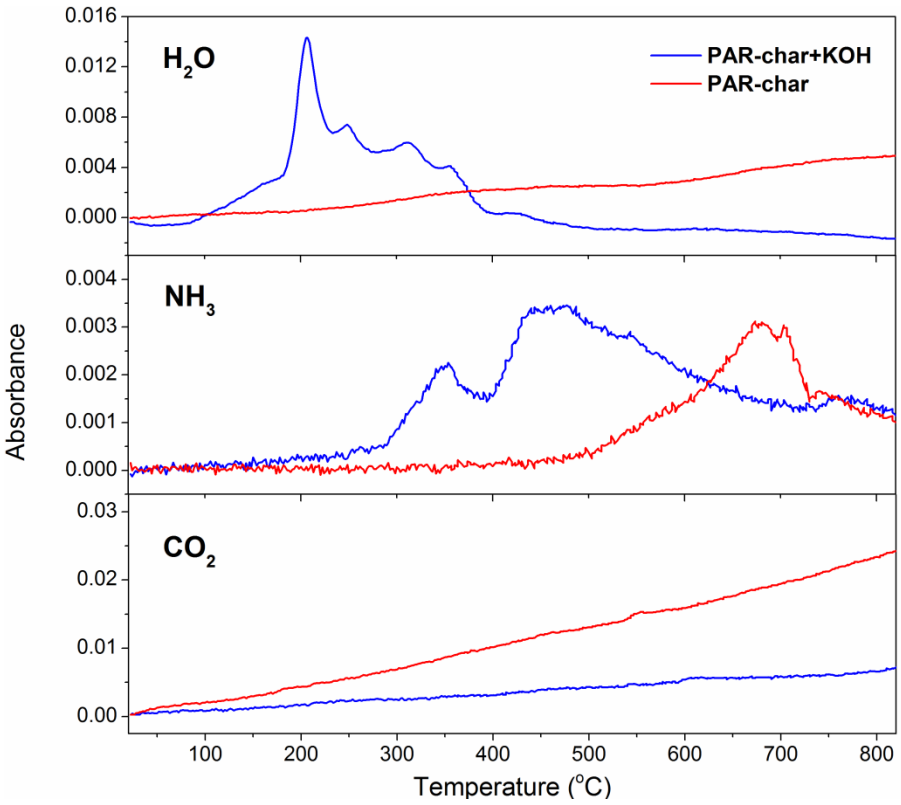

Figure S7. H_2O, NH_3, and CO_2 gaseous compounds released from pyrolysis of PAR-char+KOH and PAR-char, Related to Figure 5

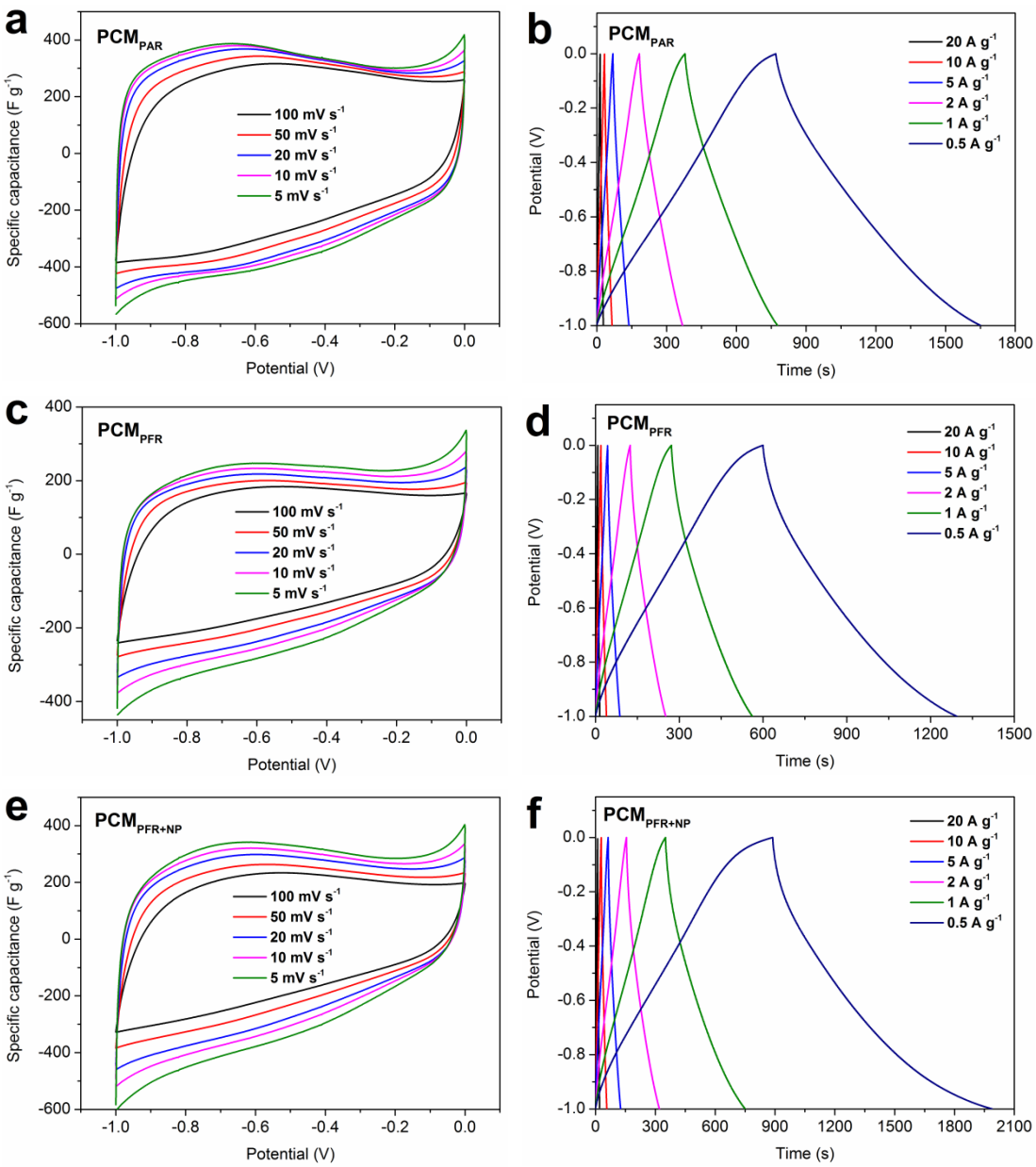

Figure S8. Electrochemical characterization of the PCMs, Related to Figure 6

(a) CV curves of PCM_{PAR} at different scan rates.

(b) GCD profiles of PCM_{PAR} under different current densities.

(c) CV curves of PCM_{PFR}.

(d) GCD profiles of PCM_{PFR}.

(e) CV curves of PCM_{PFR+NP}.

(f) GCD profiles of PCM_{PFR+NP}.

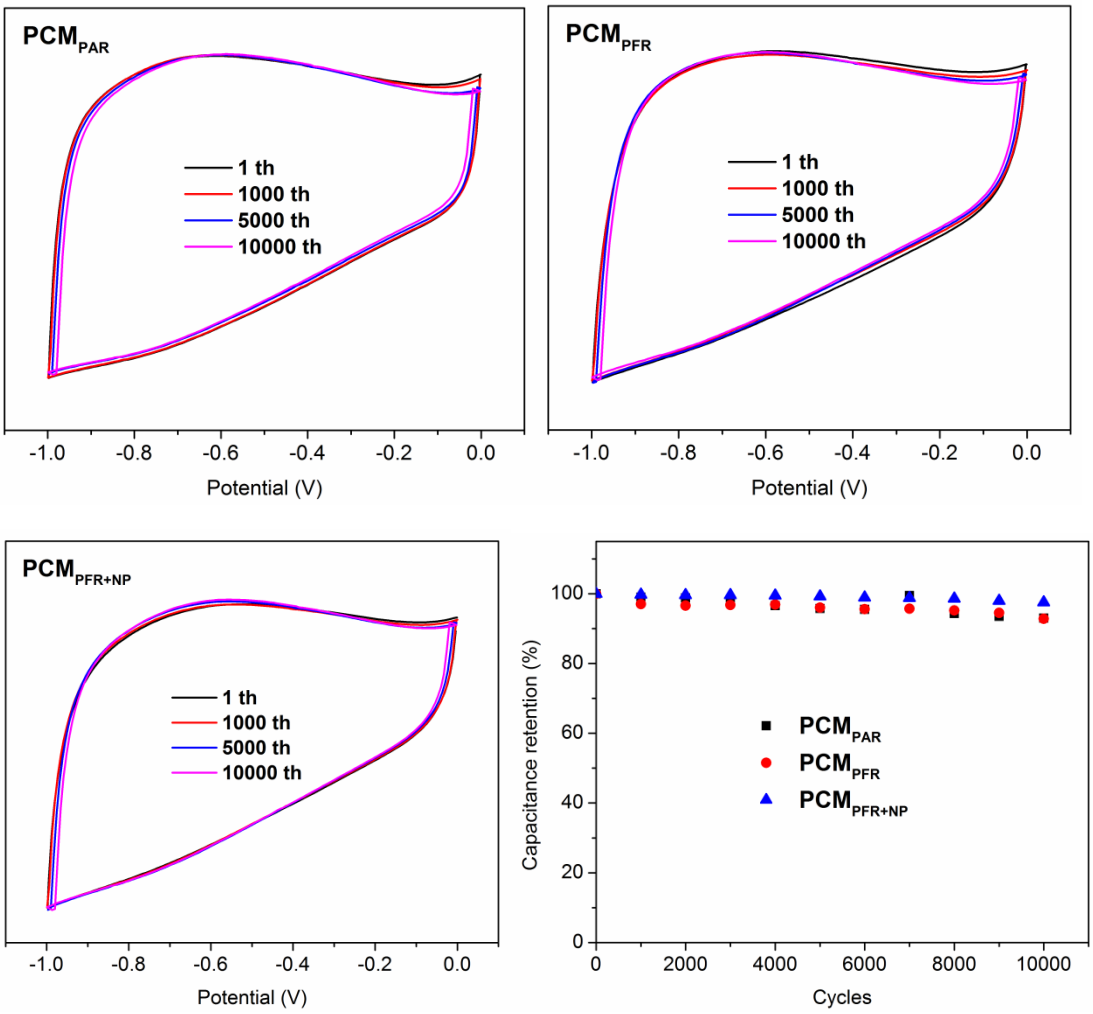

Figure S9. Cycling stability of the PCMs over 10,000 cycles at a scan rate of 50 mV s^{-1}, Related to Figure 6

The cycling performance of the PCMs was measured with 10,000 cycles. PCM_{PAR}, PCM_{PFR}, and PCM_{PFR+NP} showed capacitance retention of 93%, 93%, and 97% after 10,000 cycles, respectively.

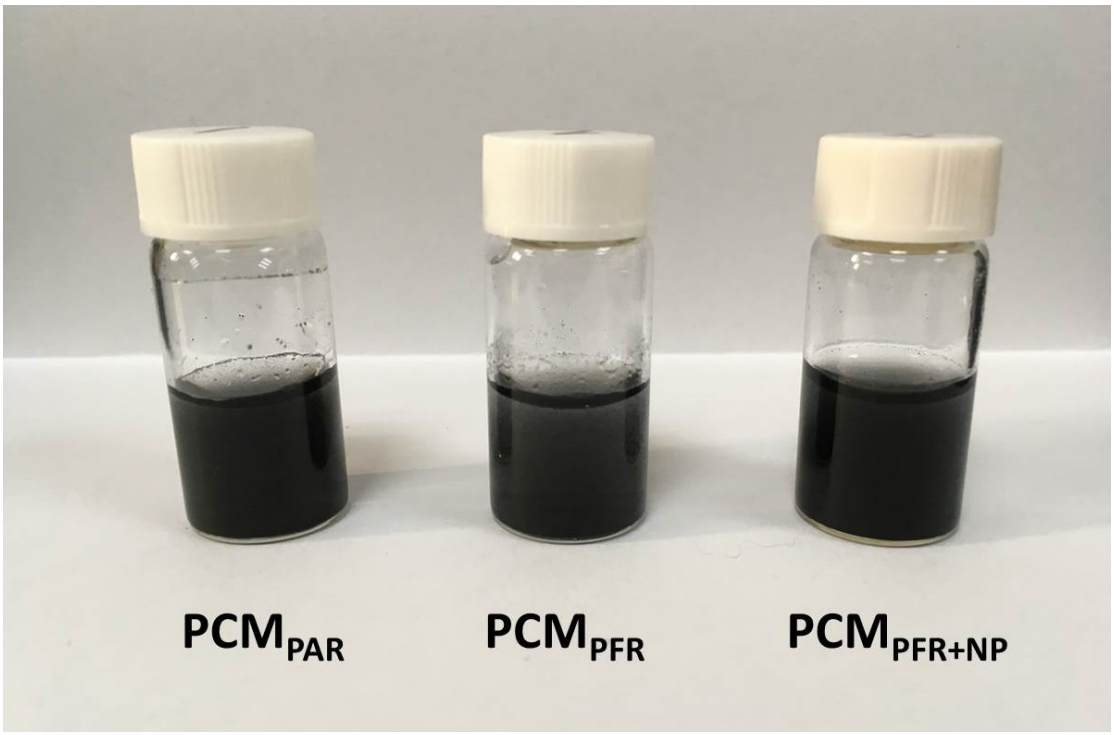

Figure S10. Photograph of PCM_{PAR}, PCM_{PFR}, and PCM_{PFR+NP} soaked in water, Related to Figure 6

PCM_{PAR}, PCM_{PFR}, and PCM_{PFR+NP} are all soaked well in water (Figure S6), which has no negative effect when used as electrode materials in aqueous solution.

Transparent Methods

Materials

The cured phenol-formaldehyde resin (PFR) was purchased from a chemical company in Anhui, China and was then ground and screened through a 100 mesh sieve. All the chemicals used in this experiment were analytically pure and without further purification.

Preparation of polyphosphamide resin

Firstly, 0.045 mol hexane-1,6-diamine and 0.09 mol triethylamine were dissolved in 200 mL dichloromethane and mechanically stirred in a 500 mL three-neck flask. Besides, 0.03 mol phosphoryl trichloride was diluted by 100 mL dichloromethane and transferred to a drip funnel. Then, the solution in the funnel was added dropwise into the flask. Continuous stirring was maintained, and the flask was cooled in an ice-water bath throughout the reaction. After stirring for 8 h, the resultant crude product was filtered and washed thrice with methanol and water successively. Then, the solid was dried in a vacuum oven at 80 ^{o}C for 24 h. Finally, the dried PAR was ground and screened through a 100 mesh sieve to collect the particles (Figure S1).

Preparation of PCMs

The PCMs were produced using PAR or PFR as carbon precursors. The synthesis of the PCMs consisted of the following steps: pre-carbonization and chemical activation. In the pre-carbonization, 5 g PAR or PFR powder was heated in an alumina crucible at 500 ^{o}C for 1 h in an argon flow at a 5 ^{o}C min^{-1} in a tube furnace.

The pyrolyzed char (denoted as C) was collected for further use.

For the chemical activation, the pyrolyzed char was first ground with powder KOH at a weight ratio of 1:4 (char:KOH). Then, the mixture was heated to 700 ^{o}C for 1 h at 5 ^{o}C min^{-1} in a tube furnace. After cooling down, the activated samples were thoroughly washed with 10 wt% HCl solution to remove the inorganic compounds and then washed with deionized water until neutral pH. Finally, the samples were dried in a vacuum oven at 80 ^{o}C for 24 h, and the obtained PCMs were denoted as PCM_{PAR} and PCM_{PFR}. To explore the effect of nitrogen and phosphorus in this process, we made a control test that contains $NH_4H_2PO_4$ as extrinsic N and P elements. In addition, the corresponding activation was held at the same heating condition at a weight ratio of 0.59:0.41:4 (PFR–char:$NH_4H_2PO_4$:KOH) according to X-ray diffraction (XRD) result. The obtained porous carbon was denoted as PCM_{PFR+NP}.

Characterization of materials

The FTIR results were recorded using a VERTEX 70 FTIR (Bruker Co., Germany) spectrometer. Thermogravimetric analysis (TGA) of PAR was performed on a TGA instrument (TGA, Q5000, V3.15, Build 263). Scanning electron microscopy (SEM, Sirion 200, FEI electron optics company, USA) and transmission electron microscopy (TEM, JEOL-2100F, Japan) were applied to visualize the morphology of the PCMs. N_2 adsorption–desorption isotherms were performed at −196 ^{o}C by using a Micromeritics ASAP 2020 (Micromeritics Gemini apparatus, ASAP 2020 M+C, Micromeritics Co. USA) to access the SSA and pore size distributions. Brunauer–Emmett–Teller (BET) method was used to calculate the SSA.

The pore size distributions were recorded based on density functional theory (DFT) method. The elemental compositions (C, H, N, and O) of the materials were determined by an elemental analyzer (VARIO EL III, Elementar Inc., Germany). The P content of the samples was determined by the molybdate–ascorbic acid method. The solid samples were first digested in concentrated HNO_3/H_2O_2 at 240 ^oC. The P concentration in the digestion solution was determined by the molybdate–ascorbic acid method on a UV–VIS spectrophotometer (UV-1800PC Spectrophotometer, Mapada Instruments, China). XRD patterns were collected with 2 θ scan range between 10° and 70° by using a X-ray diffractometer with an 18 kW rotating anode (MXPAHF, Japanese Make Co., Japan). XPS was performed using a Thermo VG-Scientific spectrometer (ESCALAB250, UK) with a monochromatized Al Ka radiation (1,486.92 eV). Raman analysis of the samples was carried out in a Laser Raman spectrometer (LabRamHR, HORIBA Jobin Yvon Co., France) with a laser radiation source operating at 514 nm and a power of 25 mW. The thermal characteristic of pre-carbonized PAR (PAR-char) and the KOH added sample (PAR-char+KOH) were analyzed by online TG-FTIR, namely, the gaseous compounds released from the carbonization were analyzed by Pyris 1 TGA (PerkinElmer) combined with FTIR spectrometer.

Electrochemical measurements

For the fabrication of working electrodes, 90 wt% PCM powders and 10 wt% of binder (polytetrafluoroethylene in methanol) were dissolved in methanol and ultrasonically dispersed to obtain a slurry. Then, the slurry was loaded on nickel foam

by coating an effective geometric area of 1×1 cm^2 and dried at 80 ^oC for 30 min. The as-prepared electrodes were then pressed under 10 MPa for 30 s and further dried at 80 ^oC overnight. The mass loading of carbon materials in electrode is 2 mg cm^{-2}. Electrochemical measurements were performed using a three-electrode system with 6 M KOH as electrolyte. Platinum wire and Hg/HgO electrode were used as the counter electrode and reference electrode, respectively. Cyclic voltammetry (CV), galvanostatical charge–discharge (GCD), and AC electrochemical impedance spectroscopy (EIS) were recorded on a CHI 760E electrochemical workstation (CH Instrument Co., China). CV curves were obtained at scan rates of 5 mV s^{-1} to 100 mV s^{-1}within the potential window from −1.0 V to 0 V (*vs* Hg/HgO). GCD measurements were carried out at current densities of 0.5 A g^{-1} to 20 A g^{-1} over a potential range from −1.0 V to 0 V (*vs* Hg/HgO). The discharge specific capacitance was calculated from the GCD curves by using Eq. 1 (Wang et al., 2012a):

$$C_m = \frac{I\Delta t}{m\Delta V} \quad (1)$$

where I (A) is the discharge current; Δt (s) is the discharge time; ΔV (V) is the voltage change after IR drop; m (g) is the mass of the PCMs in the electrode, and C_m (F g^{-1}) is the discharge specific capacitance. EIS was measured in a frequency range from 0.01 Hz to 100 kHz.

The electrochemical performance of PCM_{PAR} was also measured in a two-electrode system with two nearly identical (by weight and size) working electrodes by using a glass fiber as separator. The weight of each electrode was ~2 mg loading in 1×1 cm^2 area. The CV curves and GCD profile data were obtained in 6 M

KOH electrolyte with a CHI 760E electrochemical workstation. The gravimetric specific capacitance C_g (F g^{-1}) of a single electrode was calculated from the discharge curve after the IR drop according to Eq. 2 (Qie et al., 2013):

$$C_g = \frac{4I\Delta t}{m\Delta V} \quad (2)$$

where I (A) is the discharge current; Δt (s) represents the discharge time; m (g) is the total mass of the active material on the two electrodes; and ΔV (V) refers to the voltage change excluding the IR drop during the discharge. The energy density E_{cell} (Wh kg^{-1}) and power density P_{cell} (W kg^{-1}) were also calculated according to Eqs. 3 and 4 (Qie et al., 2013):

$$E_{cell} = \frac{C_g \Delta V}{8 \times 3.6}, \quad (3)$$

$$P_{cell} = \frac{E_{cell}}{t}, \quad (4)$$

where t (h) is the discharge time.

REFERENCES

Cai, C., Sui, Q., She, Z., Kraatz, H.-B., Xiang, C., Huang, P., Chu, H., Qiu, S., Xu, F., Sun, L., Shah, A., Zou, Y. 2018. Two dimensional holey carbon nanosheets assisted by calcium acetate for high performance supercapacitor. *Electrochim. Acta*, **283**, 904-913.

Chen, L.-F., Lu, Y., Yu, L., Lou, X.W. 2017. Designed formation of hollow particle-based nitrogen-doped carbon nanofibers for high-performance supercapacitors. *Energy Environ. Sci.*, **10**(8), 1777-1783.

Huang, C., Puziy, A.M., Poddubnaya, O.I., Hulicova-Jurcakova, D., Sobiesiak, M., Gawdzik, B. 2018. Phosphorus, nitrogen and oxygen co-doped polymer-based core-shell carbon sphere for high-performance hybrid supercapacitors. *Electrochim. Acta*, **270**, 339-351.

Miao, L., Zhu, D., Liu, M., Duan, H., Wang, Z., Lv, Y., Xiong, W., Zhu, Q., Li, L., Chai, X., Gan, L. 2018. Cooking carbon with protic salt: Nitrogen and sulfur self-doped porous carbon nanosheets for supercapacitors. *Chem. Eng. J.*, **347**, 233-242.

Qie, L., Chen, W., Xu, H., Xiong, X., Jiang, Y., Zou, F., Hu, X., Xin, Y., Zhang, Z., Huang, Y. 2013. Synthesis of functionalized 3D hierarchical porous carbon for high-performance supercapacitors. *Energy Environ. Sci.*, 6(8), 2497-2504.

Tian, W., Zhang, H., Sun, H., Tadé, M.O., Wang, S. 2017. Template-free synthesis of N-doped carbon with pillared-layered pores as bifunctional materials for supercapacitor and environmental applications. *Carbon*, **118**, 98-105.

Wang, B., Chen, J.S., Wang, Z., Madhavi, S., Lou, X.W. 2012. Green Synthesis of NiO Nanobelts with Exceptional Pseudo-Capacitive Properties. *Adv. Energy Mater.*, 2(10), 1188-1192.

Wang, J.-G., Liu, H., Zhang, X., Li, X., Liu, X., Kang, F. 2018a. Green Synthesis of Hierarchically Porous Carbon Nanotubes as Advanced Materials for High-Efficient Energy Storage. *Small*, **14**(13), 1703950.

Wang, J.-G., Liu, H., Zhang, X., Shao, M., Wei, B. 2018b. Elaborate construction of N/S-co-doped carbon nanobowls for ultrahigh-power supercapacitors. *J. Mater. Chem. A*, **6**(36), 17653-17661.

Yan, L., Li, D., Yan, T., Chen, G., Shi, L., An, Z., Zhang, D. 2018. N,P,S-Codoped Hierarchically Porous Carbon Spheres with Well-Balanced Gravimetric/Volumetric Capacitance for Supercapacitors. *ACS Sustainable Chem. Eng.* **6**(4), 5265-5272.

Yang, W., Yang, W., Ding, F., Sang, L., Ma, Z., Shao, G. 2017. Template-free synthesis of ultrathin porous carbon shell with excellent conductivity for high-rate supercapacitors. *Carbon*, **111**, 419-427.

Yang, W., Yang, W., Kong, L., Song, A., Qin, X., Shao, G. 2018. Phosphorus-doped 3D hierarchical porous carbon for high-performance supercapacitors: A balanced strategy for pore structure and chemical composition. *Carbon*, **127**, 557-567.

Zhang, S., Shi, X., Moszyński, D., Tang, T., Chu, P.K., Chen, X., Mijowska, E. 2018. Hierarchical porous carbon materials from nanosized metal-organic complex for high-performance symmetrical supercapacitor. *Electrochim. Acta*, **269**, 580-589.

Zou, K., Deng, Y., Chen, J., Qian, Y., Yang, Y., Li, Y., Chen, G. 2018. Hierarchically porous nitrogen-doped carbon derived from the activation of agriculture waste by potassium hydroxide and urea for high-performance supercapacitors. *J. Power Sources*, **378**, 579-588.